Article

Enhancing Polyantimonic-Based Materials' Moisture Response with Binder Content Tuning

Sofia Mendes [1], Olga Kurapova [2] and Pedro Faia [1,*]

1   CEMMPRE—Electrical and Computer Engineering Department, University of Coimbra, FCTUC, Polo 2, Pinhal de Marrocos, 3030-290 Coimbra, Portugal; uc2002123458@student.uc.pt
2   Physical Chemistry Department, Saint Petersburg State University, Universitetskya Nab. 7/9, 199034 Saint Petersburg, Russia; o.y.kurapova@spbu.ru
*   Correspondence: faia@deec.uc.pt; Tel.: +351-239796200

Abstract: Humidity sensors are of huge importance in diverse domains. Several types of materials present a moisture-sensing capacity; however, frequently, their electrical response does not display time stability. Due to its high thermal stability, high ionic conductivity, and different conduction mechanism contributing to its overall conductivity, polyantimonic acid (PAA) is seen as a promising material for humidity-sensing devices. In the present work, crystalline PAA was obtained via a simple and safe hydrolysis technique using $SbCl_3$ as a precursor. Bulky sensor samples were produced using different amounts of polyvinyl alcohol (10–20 wt.% PVA) as a binder. The obtained PAA solid sensors were tested at room temperature (RT) in order to evaluate their moisture detection/measuring ability in the relative humidity range 0–100%; the evaluation was carried out with electrical impedance spectroscopy. The sample's structure and morphology were studied using diverse experimental techniques (porosimetry, scanning electron microscopy, X-ray diffraction analysis, and thermogravimetry analysis, etc.). The sensors' electrical response was in line with the found structural and morphological features. The slope of the resistance variation with an RH percentage concentration between 1 kΩ and 1.5 kΩ was noted for all sensors (showing no changes with time) in the interval between 30 and 100% RH. A good repeatability and reproducibility of the evaluated sensors' electrical response was observed: the ones that displayed a higher sensitivity were the ones with a high PVA binder content, higher than previously published results for PAA, as well as a very good time stability along the time and low hysteresis.

Keywords: humidity sensing; electrical impedance spectroscopy; polyantimonic-based sensors; PVA; model circuit

1. Introduction

Humidity is a problem of great importance in several areas of research and production, such as pharmaceutical, food, or electronics industries [1–3], as the needs of the mentioned industries are sufficient to justify continuous interest in the development of enhanced humidity sensors.

Among the requirements that allow materials to be appropriately employed in humidity-measurement applications are their high sensitivity, fast response time, reproducibility, low cost, and low hysteresis, not to mention that they should be capable of operating along a widespread range of temperatures and moisture concentrations. In recent years, diverse materials have been evaluated regarding their humidity sensitivity, such as conductive polymers [4], carbon-based materials [5], metal oxides [6], metal oxide composites [7], mxenes [8], and cellulose-based materials [9]. More recently, ceramics like hallosyte nanotubes [10], attapulgite [11], and sepiolite nanofibers [12] have also been successfully used and reported for humidity sensing. They have been shaped in different forms [13–15] and fabricated with diverse procedures [2].

Water vapor adsorption on the surface of the sensor material due to chemisorption and physisorption and due to capillary condensation processes along the material's porous structure are the main mechanisms behind all electrical humidity sensors [2]. Electrical humidity sensors' working principle can be based on the electronic and/or on the ionic conductivity contributions of the materials used for their fabrication to the overall electric response to moisture. Among the mentioned contributions, the Grotthuss chain reaction one, which is of an ionic nature, is one of the most relevant, particularly for protonic conductive materials [16]; for instance, $Sb_2O_5 \cdot nH_2O$, $ZrO_2 \cdot nH_2O$, and $SnO_2 \cdot nH_2O$ display ionic conduction [17]. Therefore, protonic-type conductive materials are great candidates to be used in moisture sensors. Among them is polyantimonic acid (PAA).

The electrical response to the moisture of a humidity sensor can be modified by manipulating its structure and/or molecular organization. Altering sensing material production steps allows for defining its structural organization (making it more crystalline or more amorphous) and consequently its porosity and overall contact surface with moisture. A sensor with a larger contact surface is capable of higher interaction with water molecules in the environment in which it is located. The porosity of a sensor favors its response to humidity, particularly involving mesoporous region pores. However, there is a limit to this porosity, as a greater volume of pores, particularly large pores, contributes to the sensor deterioration. Besides their sensitivity, two other important features of humidity sensors are the repeatability and hysteresis behavior of their response.

Polyantimonic acid is an inorganic compound that has acquired many names over the years, ranging from antimonic acid [18–20] to antimony oxide hydrates [21], hydrous antimony oxide [17], hydrated antimonic acid [22], hydrated antimony pentoxide [20–24], and polyantimonic acid (PAA) [22,25,26]. The chemical composition of PAA has given rise to discussion and disagreement from the beginning, and to date, there is still no consensus. In the 1920s, Jander and Simon [27] reported that the structure of antimonic acid divided opinions and raised doubts, giving rise to sometimes contradictory results, a situation continuously recorded over the years of study of this compound [17,20,28–30]. The difficulty in defining a chemical formula as a unique formula for PAA is related to the fact that this is a compound whose number of adsorbed water molecules is quite variable, and the pure crystalline form is extremely difficult to obtain.

PAA is an inorganic compound with several interesting characteristics; namely, it is an excellent proton conductor [17,31–33], and it has a good ion-exchange capacity [21,22,34,35], and despite the variation in the amount of water in its structure, it is a compound with a good thermal and mechanical stability [20,30]. These characteristics make PAA a great candidate to be used in humidity-sensing applications. However, membranes or pellets produced with pure PAA are not viable because they are brittle and mechanically unstable. Thus, it is always necessary to add a binder so that it is possible to obtain more stable membranes that do not become brittle when handled [36,37]. The study of PAA has already been carried out in conjunction with some ligands such as polyvinylidene fluoride (PVDF) [30,38], polytetrafluoroethylene (PTFE or Teflon$^{®}$) [39], and fluoroplastic [40].

In a previous paper by the authors [40], a comparative analysis between some of the aforementioned characteristics was performed between several materials and fabrication routes reported in the literature, which allowed for highlighting the benefits and drawbacks of the material and fabrication route chosen by the authors. The main ones are concerned with hysteresis performance and low fabrication costs [41–44]. All things considered, the incorporation of polyvinyl alcohol, PVA, as a binder did not decrease the conductivity of the material (contrarily to what occurred in a work by Burmistrov et al. [32], where the usage of PVA as a binder gave origin to materials with dielectric properties).

Several studies, even considering that the number of water molecules is variable, have given rise to similar results regarding the level of the structural organization of the crystal, having obtained a cubic organization of pyrochlore of the $Fd\bar{3}m$ group with the lattice size a ≈ 10.38 Å [20,24,45,46]. The extent of PAA crystallization varies according to the number of water molecules in its structure [20], a fact verified with an X-ray diffraction analysis,

XRD, in a study of PAA samples for different ageing states. The obtained PAA, mostly amorphous, displayed wide and weak peaks; however, as the samples were dried and aged, the characteristic peaks intensified and became narrower [47].

In an attempt to describe the mechanisms of proton conduction in PAA crystalline-form samples, the existence of a nucleus formed by $[Sb_2O_6]^{2-}$ in an octahedron, connected by vertices where the hexagonal channels contain H_3O^+ ions and adsorbed water molecules, was proposed in a recent work [46]. It should be noted that for this case, the formula considered for the PAA was $H_2Sb_2O_6 \cdot n\ H_2O$ (2 < n < 5) [46].

Resuming, PAA-based materials are great candidates to be used in moisture sensors as the different mechanisms of proton transfer are realized.

In the present work, the authors propose the use of a new binder with the expectation of enhancing the structural properties of the solid samples, a combination of PAA with *Poly(vinyl alcohol)*, and PVA, with the consequent improvement of their electrical response to humidity changes, regarding not only sensitivity but also time stability and a low hysteresis.

2. Materials and Methods

2.1. Crystalline PAA Powder Preparation

Polyantimonic acid was synthesized using the technique adopted from [48,49], including the oxidation of Sb(III) to Sb (IV) as the first step and hydrolysis of an obtained Sb (V) solution as the second step. Antimony (III) chloride ($SbCl_3$, Alfa Aesar, 99.0%, Kandel, GmbH, Germany) was used as a precursor. Powdered $SbCl_3$ was dissolved into 12 M of hydrochloric acid (HCl, Alfa Aesar 36%, Kandel, GmbH, Germany). For this, the HCl solution was added drop by drop to $SbCl_3$ under magnetic stirring at 200 rpm at room temperature, RT. Subsequently, the excess of a 6 wt.% solution of hydrogen peroxide, H_2O_2 (Alfa Aesar, Kandel, GmbH, Germany), was dropwise added to the previously obtained solution at room temperature for carrying out the oxidation of Sb(III) into Sb(V). After, the reaction mixture was left under intensive stirring (400 rpm) for at least 1 h to fulfil Sb (III) oxidation. To complete the decomposition of hydrogen peroxide, the obtained solution was heated up to 60 °C under intensive stirring (325 rpm) for 2 h.

In the next step, the hydrolysis of Sb(V) was performed to obtain PAA powder. The solution of $SbCl_5$ was slowly added dropwise to a large volumetric excess of deionized water (about 1:50, Alfa Aesar ACS grade, Kandel, GmbH, Germany) under stirring at RT. A white precipitate of amorphous PAA was formed. The precipitate was left together with the mother solution to achieve crystallization at RT for 7 days. After, the solution was filtrated using a Büchner funnel. The resulting precipitate was washed with distilled water until a neutral pH was reached. The washing waters were tested for the presence of chloride ions using a reaction with a silver nitrate solution ($AgNO_3$, Alfa Aesar ACS grade, Kandel, GmbH, Germany). The procedure of washing was repeated until the negative test was obtained.

The obtained crystalline PAA was placed in a muffle furnace on top of filter paper at 60 °C until no weight change was observed (at least 8 days). Then, the resulting product was grinded (Retsch Mixer Mill, MM 2000, Haan, GmbH, Germany), in a stainless-steel holder with two stainless-steel balls, for 10 min. Here and further in the text, crystalline PAA powder is referred to as P0.

2.2. Binder Preparation

In this work, poly(vinylalcohol) PVA (Merck-Schuchardt 72000, KGaA, Darmstadt, Germany) was chosen as the binder. To avoid agglomeration, PVA was slowly added to deionized water in small portions under magnetic stirring at RT. The obtained gelatinous solution was then heated up to 80 °C under constant magnetic stirring until no granulation or agglomerates of undissolved PVA were observed. Then, it was left for 24 h to eliminate the bubbles produced in the agitation process.

2.3. Solid Electrolyte Preparation

Tablets with dimensions of $10 \times 7 \times 3$ mm were produced in different proportions of PAA and PVA, namely 80:20, 85:15, and 90:10. The respective amounts of each compound were weighed and mixed in respective proportions. Then, in order to obtain a better homogenization of the mixture, they were grinded in a mixing mill (Retsch Mixer Mill, MM 2000, Haan, GmbH, Hamburg, Germany) inside a holder of stainless steel with stainless-steel balls for 10 min. The solid samples were obtained via uniaxial pressure with an initial force of 70 kgf/cm^2 and 1 min of exposition at a force of 30 kgf/cm^2 for 30 min. After unmolding, solid samples were left to dry at the ambient conditions for at least 5 days. From here, ahead, the samples with the proportions of 80:20, 85:15, and 90:10 in weight will be designated PP20, PP15, and PP10, respectively.

2.4. Structure Characterization of Samples

Regarding structural and morphological characterization, several techniques were used. Morphology was analyzed with Field-Emission–scanning-electron-microscopy, FE-SEM (Zeiss Merlin, Carl Zeiss QEC GmbH, Peine, Germany, accelerating voltage of 2 kV), and using Transmission Electron Microscopy, TEM (JEOL JEM2100, JEOL, Tokyo, Japan, an electron beam energy of 200 keV, equipped with energy dispersive spectroscopy, EDS). Bulky sensors' chemical composition was examined with X-ray energy dispersive spectroscopy, EDS, coupled to FE-SEM (Oxford EDS X-MAX^N 20 spectrometer, accelerating voltage of 10 kV, Oxford Instruments, Wycombe, Buckinghamshire, UK). Regarding the analysis of the valence states of antimony as well as the presence of Sb^{3+} in the samples, it was carried out by means of X-ray Photoelectron Spectroscopy, XPS (ESCALAB 250Xi, Thermo Fisher Scientific, Waltham, Massachusetts, USA, pressure less than 5×10^{-10} mbar, monochromatic Al Kα radiation, hv = 1486.68 eV, 220 W, 14.6 kV, spot size of 650 μm). For evaluating the phase compositions of the prepared PAA powder and of the solid sensors, an X-ray diffraction analysis, XRD, was used (diffractometer Philips X'pert, Malvern Panalytical, Malvern, United Kingdom, Bragg–Brentano geometry, using Cu Kα irradiation, 1.5406 Å, scanning speed of 0.02°/min, 2θ range of 10–100°). For evaluating samples' pore distribution, Mercury porosimetry was utilized (AutoPore IV, model 9500, Micrometrics, Ottawa, Canada, in the range of 0.5 to 33.000 absolute psia).

2.5. Electrical Response Measurements

To assess samples' electrical response to moisture changes, Complex impedance spectroscopy, CIS (Agilent 4294A, Agilent, Santa Clara, CA, USA), was used in the frequency interval between 400 Hz and 40 MHz (frequencies were conducted with logarithmic increments of the frequency). It must be mentioned that since the Agilent equipment has inbuilt Kramer–Krönig transformations, the data integrity of the obtained measures was observed. For the measures, the samples were placed inside a closed chamber (which had a volume of approximately 6.5 L), on top of a support equipped with measuring contacts. The temperature inside the chamber was kept at around 25 °C; using a temperature controller, GEFRAN model 1000, that runs a Proportional Integrative Derivative, PID, algorithm, the temperature was regulated with an accuracy greater than 1 °C. In the support holding the solid samples, two other types of elements were attached, a type K thermocouple and two heating elements, all connected to the temperature controller and used by the controller for achieving temperature regulation. All measurements were carried out at room temperature, RT, while RH was varied between 0 and 100% RH. The diverse RH concentrations were attained by mixing, in the wanted fractions, dry synthetic air with water-saturated air (fully humidified air was obtained by passing dry synthetic air through a water bubbler). By mixing in the desired volumetric proportions of wet and dry air in a mixer, both controlled by independent mass flow controllers, the diverse RH concentrations were obtained; using the gas chromatography technique, a gas chromatograph, GC (GC1000, DANI), was used to check and validate the desired RH concentrations continuously. Throughout all electrical measures, a flow rate of 5 L/h of all tested RH concentrations was maintained for at least

90 min (defined to assure that the chamber content was renewed). Using gold ink (Gwent Group, Gold Polymer Electrode Paste C2041206P2) and utilizing a mask, a pair of gold electrodes were printed onto the extremities of the upper surface of each sample; before making the measures, the printed gold electrodes were cured at 80 °C for 60 min. For all compositions, two specimens were characterized, and for each one, three acquisition runs were performed for every RH percentage measure; the data displayed are always the mean values of the three runs for each measure for all samples of all compositions.

3. Results and Discussion

3.1. Morphological and Structural Analysis

The XRD patterns obtained for the pure PAA; PP0; and the bulk samples PP10, PP15, and PP20 are shown in Figure 1. The XRD pattern of PP0 corresponds to a single phase of well-formed crystalline $Sb_2O_5 \cdot 3H_2O$ (ICCD card 84-0303), which possess a pyrochlore-type structure with the space group $Fd\bar{3}m$. No traces of any side phases such as Sb_2O_3, Sb_2O_5 (monoclinic), or SbO_2 or $Sb_2O_4 \cdot n H_2O$ are observed. It can be concluded that the developed synthesis technique allows for obtaining the desired crystalline modification of Sb_2O_5.
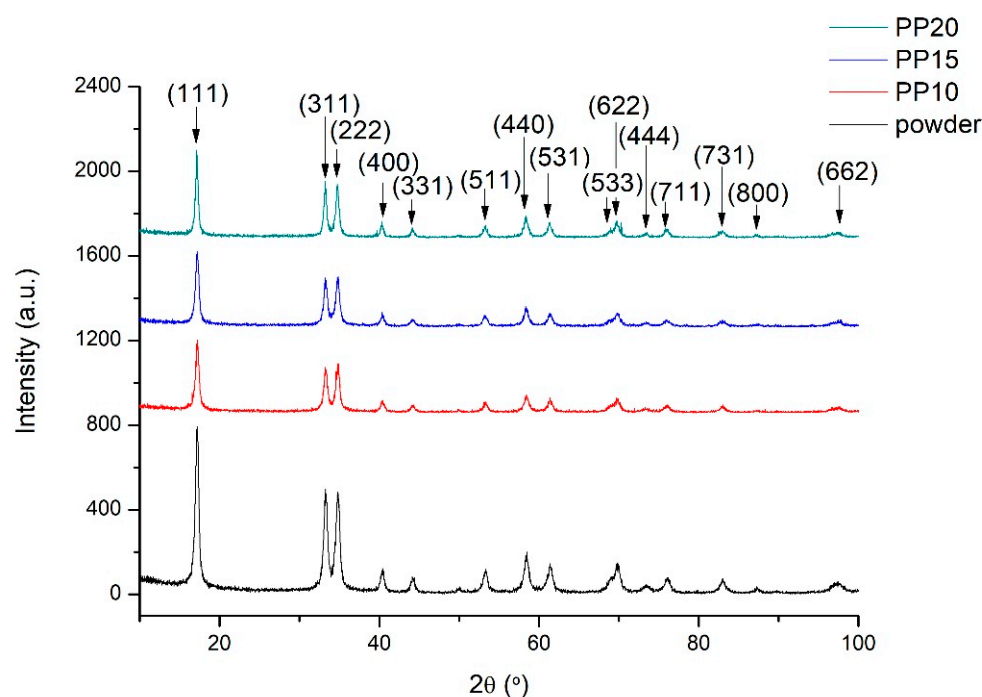

Figure 1. XRD analysis of the synthesized PAA powder and of the bulk solid-state samples.

The incorporation of 10–20 wt.% of PVA decreases the intensity of the peaks in the XRD patterns of PP10, PP15, and PP20 when compared to the ones observed for pure PAA. In the case of PP20, the additional peaks with low intensities appear at 2θ = 39.663, 68.912, and 70.313° in the XRD pattern, corresponding to the low crystalline binder, PVA.

Since the detection limit of the XRD technique is 3–5 wt.%, the synthesized PAA powder was subjected to an XPS analysis to confirm the complete oxidation of Sb (III) to Sb(V) during the synthesis. The XPS data are presented in Figure 2. As seen, the sample contains peaks corresponding to Sb and O. A low admixture of carbon, characterized by the C1s peak with a binder energy of 285 eV, is also present in the sample. It is likely due to some amount of CO_2 adsorbed on the surface of $Sb_2O_5 \cdot 3H_2O$ powder. As seen, the $Sb3d_{5/2}$ peak with the binding energy of 531.5 eV is overlapped with the O1s peak. So, the $Sb3d_{3/2}$ peak is typically used to identify the oxidation state of antimony, which typically is found at the binding energy of 542 eV [50]; see Figure 2 inset. To verify the oxidation state of Sb, the sample was sputtered with argon, promoting the reduction of Sb^{5+} ions to Sb^{3+} ions. As seen in Figure 3, after sputtering with Ar, the intensity of the O1s peak at 530.95 eV

dropped. The fitting of the spectrum of the treated sample shows the presence of two peaks at low binding energies, 532.25 eV and 541.5 eV, which are attributed to low oxidation states of the Sb ions below +5. The experiment with reduction by Ar confirms that PAA, after synthesis, contains only Sb^{5+}, as required for sensor development; consequently, the complete oxidation of antimony was confirmed.
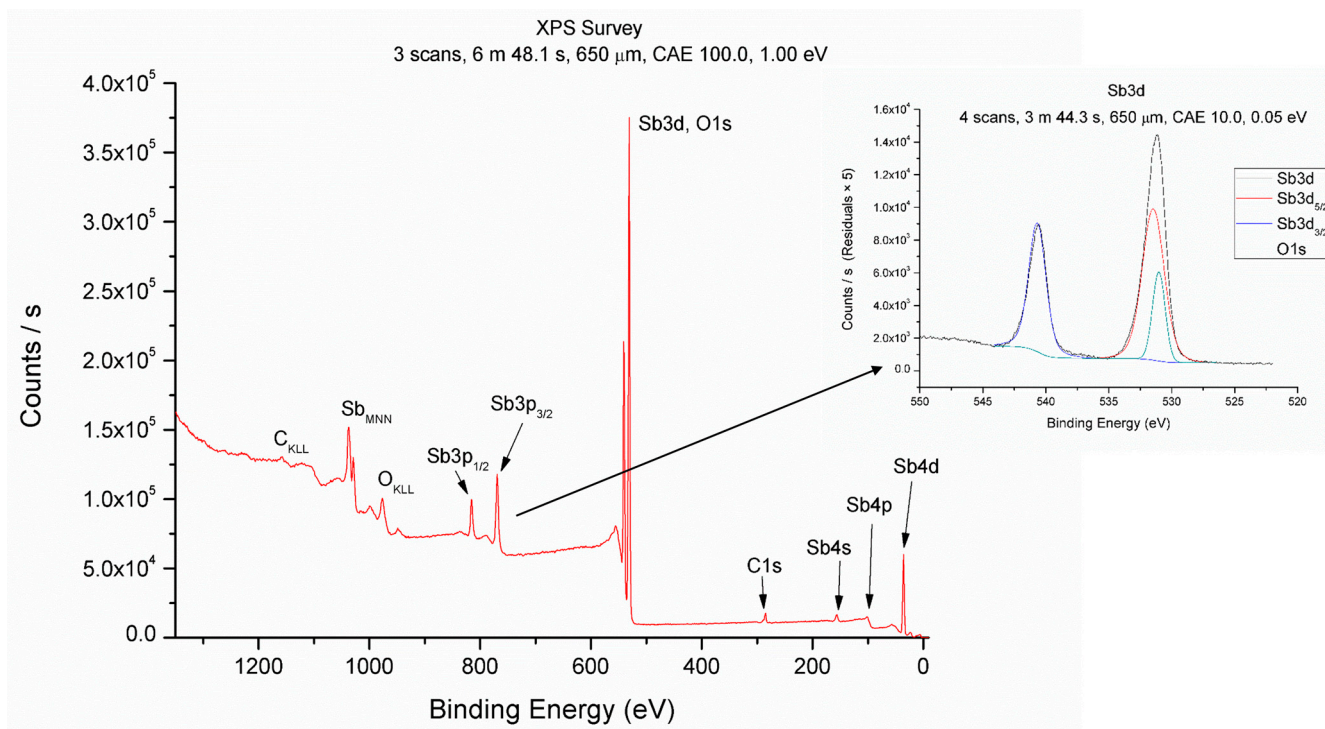
Figure 2. XPS analysis of the synthesized PAA powder.
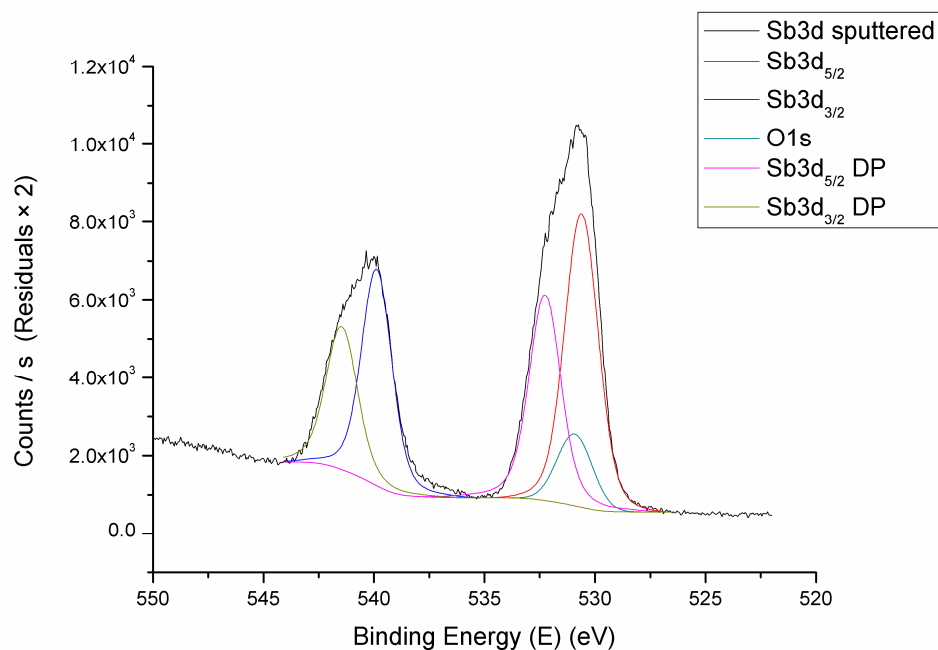
Figure 3. Sb3d and O1s peaks after sputtering with argon, Ar, ions.

Figure 4 shows high-resolution SEM images of the surfaces of the samples (Figure 4a–c), as well as their cross-sections (Figure 4d–f). The solid electrolyte is composed of agglomerated nanosized PAA particles. As seen from Figure 4c,f, the individual PAA particles possess the characteristic shape of cubic crystals, indicating that the desired pyrochlore

structure was obtained during the synthesis. By comparing the surface images obtained for PP10, PP15, and PP20 samples, one can see that the increase in binder content induces (a) a decrease in the agglomeration degree of PAA particles in the samples and (b) an overall roughness and more uniform structure of the PP20 sample. The structural cross-section images are similar to the ones observed for surfaces. The overall decrease in the agglomeration and structure uniformization is expected to lead to a more uniform pore volume distribution and a decrease in pores with higher dimensions.
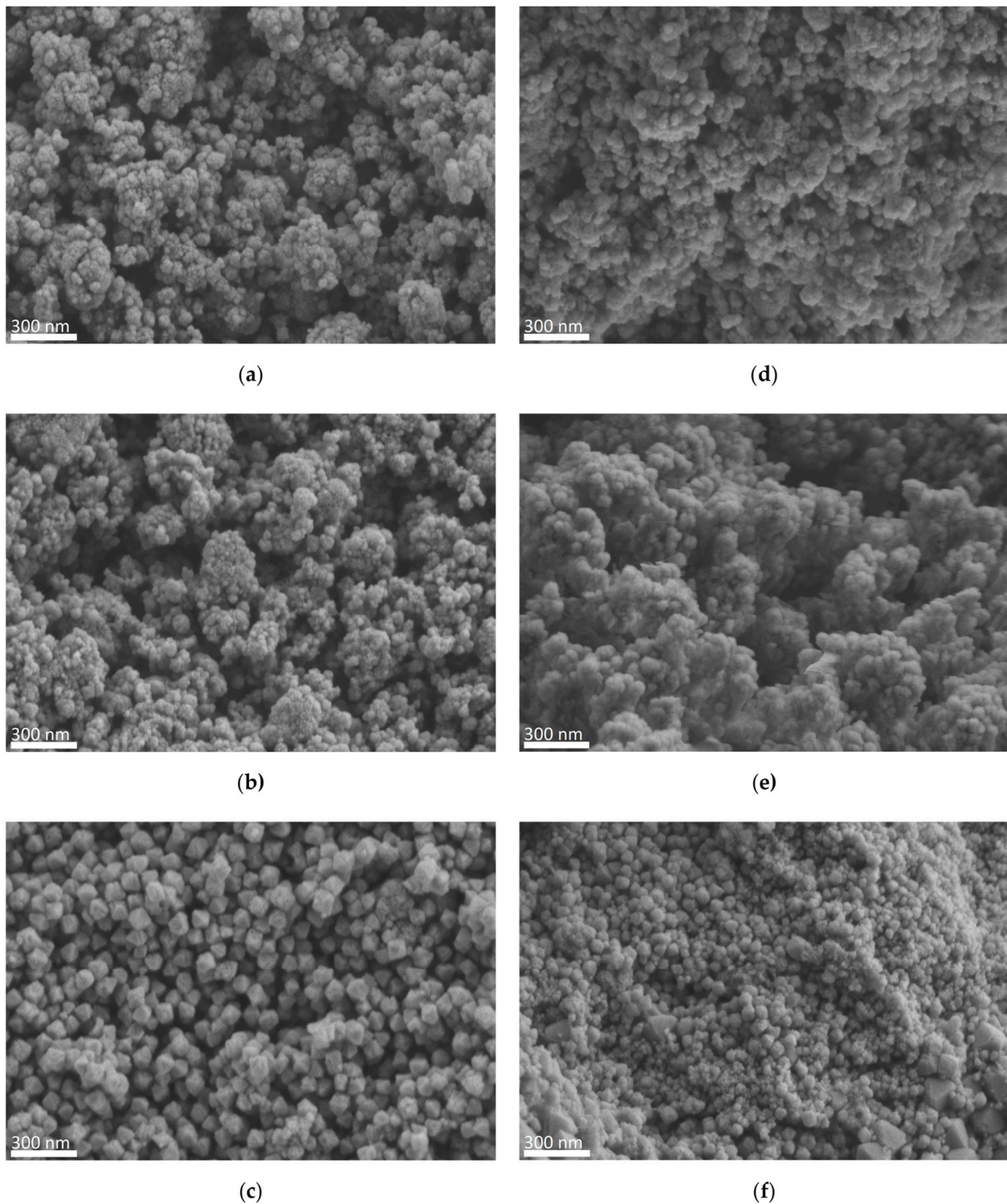

Figure 4. High-resolution SEM images: surfaces of (**a**) PP10, (**b**) PP15, and (**c**) PP20 samples; cross-sections of (**d**) PP10, (**e**) PP15, and (**f**) PP20 samples.

These assumptions are validated with the porosimetry study performed. The results are displayed in Figure 5. The overall pore volume values decrease from 0.1983 mL/g for PP10, to 0.1511 mL/g for PP15, and to 0.1086 mL/g for PP20. The trend is in accordance with the particle agglomerates' decrease. At the same time, the volume of pores in the mesoporous region increases. The average pore diameters shift from 0.0466 to 0.0151 μm for PP10 and PP20, respectively. Remarkably, PP15 possesses an intermediate pore structure; a multimodal pore distribution is observed, and the average diameters almost coincide with the ones for PP10 and PP20.
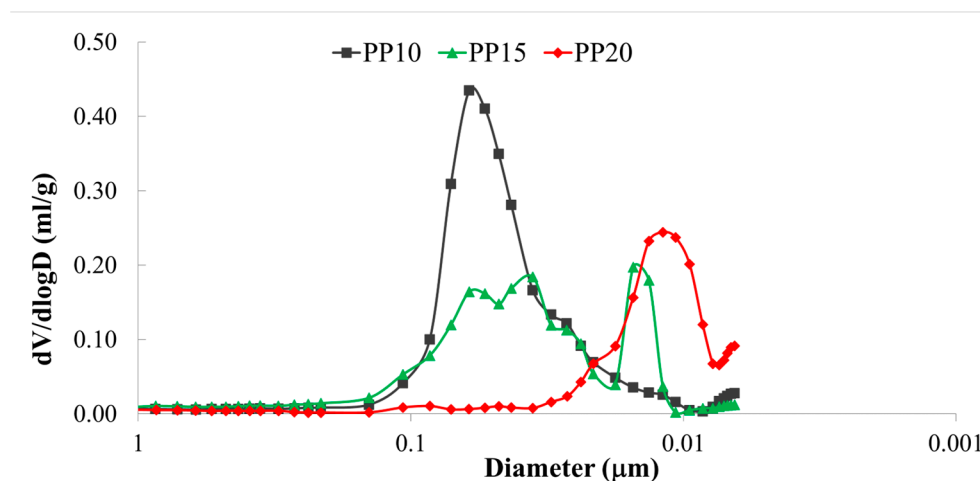
Figure 5. Porosimetry analysis of PP10, PP15, and PP20 samples.

It can be concluded that the PP20 sample displays better morphological properties, i.e., a higher mesoporosity and smaller volume of pores. Consequently, it is expected to have a higher overall contact surface between moisture and the sensing surface and to favor the enhancement of the electrical response of materials. So, PP20 was further evaluated with TEM (Figure 6). From Figure 6, the already discussed existent and significant mesoporosity of sample PP20 is once again observed (the dimension of the voids in the TEM image is in the range between 50 and 100 nm). In addition, it consists of particles with sizes in the nanometer range, consolidated with each other by the PVA binder. An Electron Energy Loss Spectroscopy analysis, EELS, performed along with TEM, allowed for confirming that the sample is mainly composed of antimony, Sb, mostly in the oxide form (Cr and Cu were also found in the analysis, but they belong to the surrounding structural parts of the microscope).

Figure 6. TEM of PP20 sample: (**a**) 30,000× amplification; (**b**) 300,000× amplification.

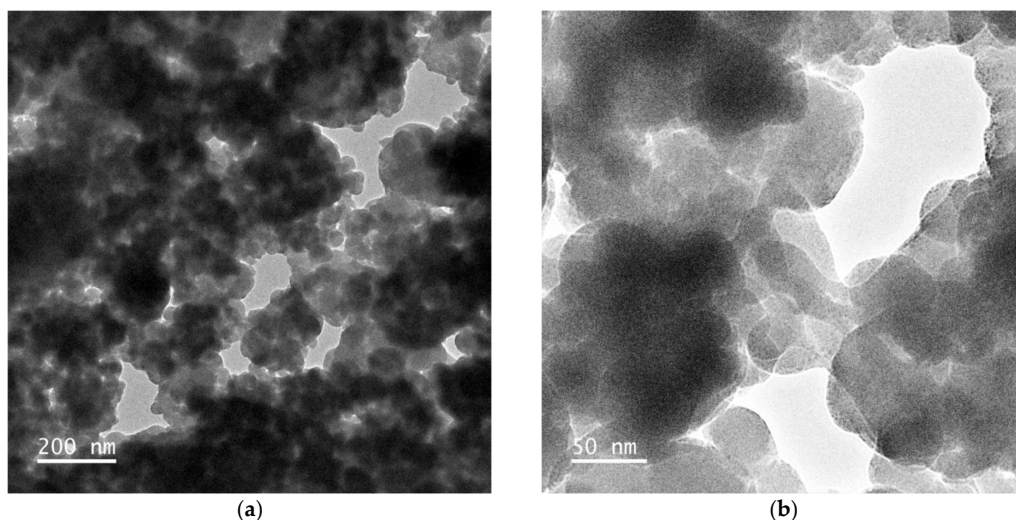At last, and to additionally assess samples' structural stability, PP0, PP10, and PP20 were evaluated with thermogravimetry (Figure 7). As seen, the TG curves are characterized by several steps of mass loss. All curves do not exhibit a mass loss up to 60 °C. A slight mass loss of about 5 wt.% is seen for all samples in the region 60–170 °C due to water losses by PAA. A considerable stepwise mass loss continues up to 300–330 °C, indicating a water loss, and the stability of bulk samples continues up to 300 °C (only for higher temperatures; a weight loss of the solid samples in comparison with the fabricated powder starts to differ in consonance with the amount of binder content) [36,45]. Once, as moisture sensors, the solid samples operate at the ambient temperature, the obtained results prove their structural stability. In conclusion, the produced sensors were obtained with a low-cost synthesizing procedure, display promising morphological properties for moisture electrical evaluation (verified with SEM, TEM, and porosimetry), and exhibit phase stability (XRD and XPS).
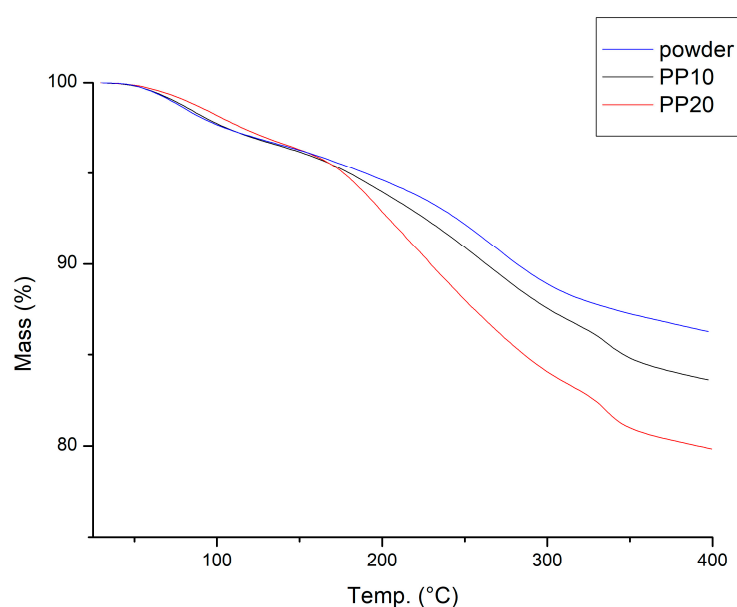

Figure 7. Thermogravimetry analysis, TGA, of the powder, and of PP10 and PP20 samples.

3.2. Electrical Behavior

In Figure 8, the Nyquist curves obtained for the PP10, PP15, and PP20 samples, recorded for an RH increase from 0 up to 100%, are represented. The low- and high-humidity ranges were separated into two graphs, allowing a better visualization of the sample's behavior with an RH increase. Using an inspection of the Nyquist diagrams, it can be stated that the samples exhibit a significant impedance variation with RH concentration. In addition, they all display a continuous increase in the real and imaginary components of the impedance with an RH rise to around 30%; then, with RH increasing further above this value, they all display a decrease in both real and imaginary parts of the impedance. The plots allow the authors to state that PAA samples exhibit mainly an n-type electrical behavior (in the named high-humidity range), displaying, however, a *p*- to n-type transition for RH values around 30% (in the low-humidity range, they exhibit *p*-type behavior). This fact is not uncommon to occur when chemisorption is complete, and physisorption starts to take over. Additionally, the visible semicircles in the plots prove the existence of electronic-nature contributions to the overall electrical response of the sensors to RH. At the same time, ionic ones are also present, characterized by the visible Warburg-type component (the straight line in the spectra with a 45° slope). Warburg-type contributions are due to diffusion processes occurring in the interface between the material surface and the measuring electrodes, along the material surface, and in the pores that are gradually filled with water molecules.
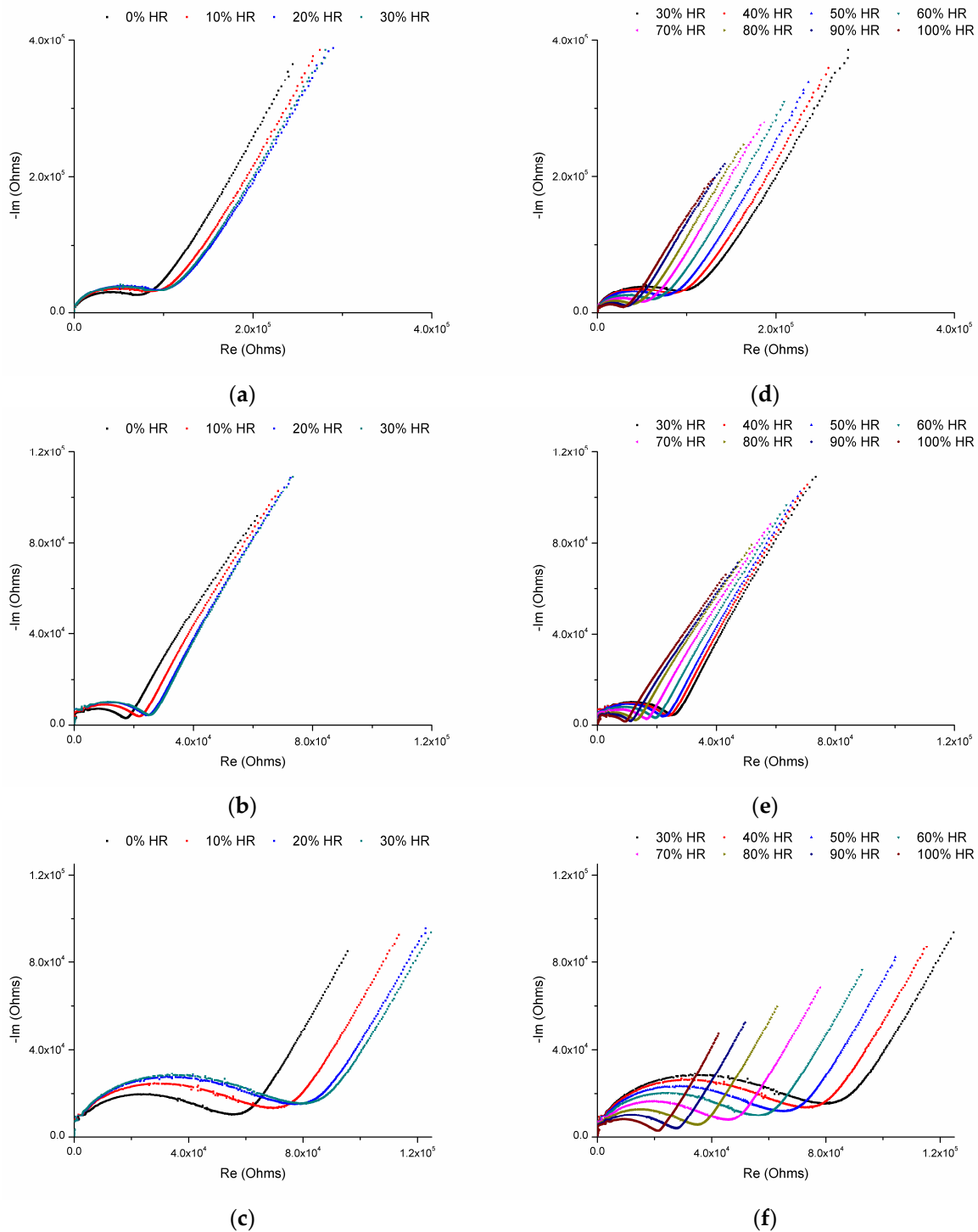
Figure 8. RH-variation Nyquist plots: (**a**–**c**) low-humidity range for PP10, PP15, and PP20 samples, respectively; (**d**–**f**) high-humidity range for PP10, PP15, and PP20 samples, in this order.

Regarding the construction of electrical model circuits of the behavior of polycrystalline materials based on Bauerle's theory [51,52], a large semicircle at high frequencies holds for the conductivity of grain boundaries, while a small one stands for the conductivity of samples' bulk (grain and grain agglomerates). For the present samples, a unique semicircle is detected for the lower frequencies, and typically the authors would be directed to conclude that a single contribution exists. This is not necessarily true; indeed, existing conduction processes possessing relaxation frequencies close to each other will be superimposed in Nyquist plots. Since the dimension of the semicircle decreases with the

RH concentration, it may be concluded that the influence of the electronic contributions is more relevant for the lower RH concentrations when chemisorption dominates. So, in conclusion, the overall electrical response of all PAA samples displays both electronic and ionic contributions along the entire RH range, where the ionic ones dominate. Additionally, the authors can conclude, by observing the obtained spectra, that sample PP20 is the one that exhibits a higher humidity response; indeed, it is the one for which the Nyquist plot curves show a more significant amplitude variation over both the real and imaginary axis regarding RH changes, being more significant than the ones corresponding to the real contribution to the overall impedance.

Besides that, it is observable that all three compositions display around the transition between low and high RH regions (the high-humidity region is defined as the one where physisorption starts to take place, which typically occurs at RHs between 20 and 40%), a *p*- to n-type conduction transition. The transition and the fact that sample PP20 has the highest sensitivity are highlighted in Figure 9, where the calculated impedance samples' moduli over the entire measured RH range are plotted for diverse excitation frequencies.

(a)

(b)

(c)
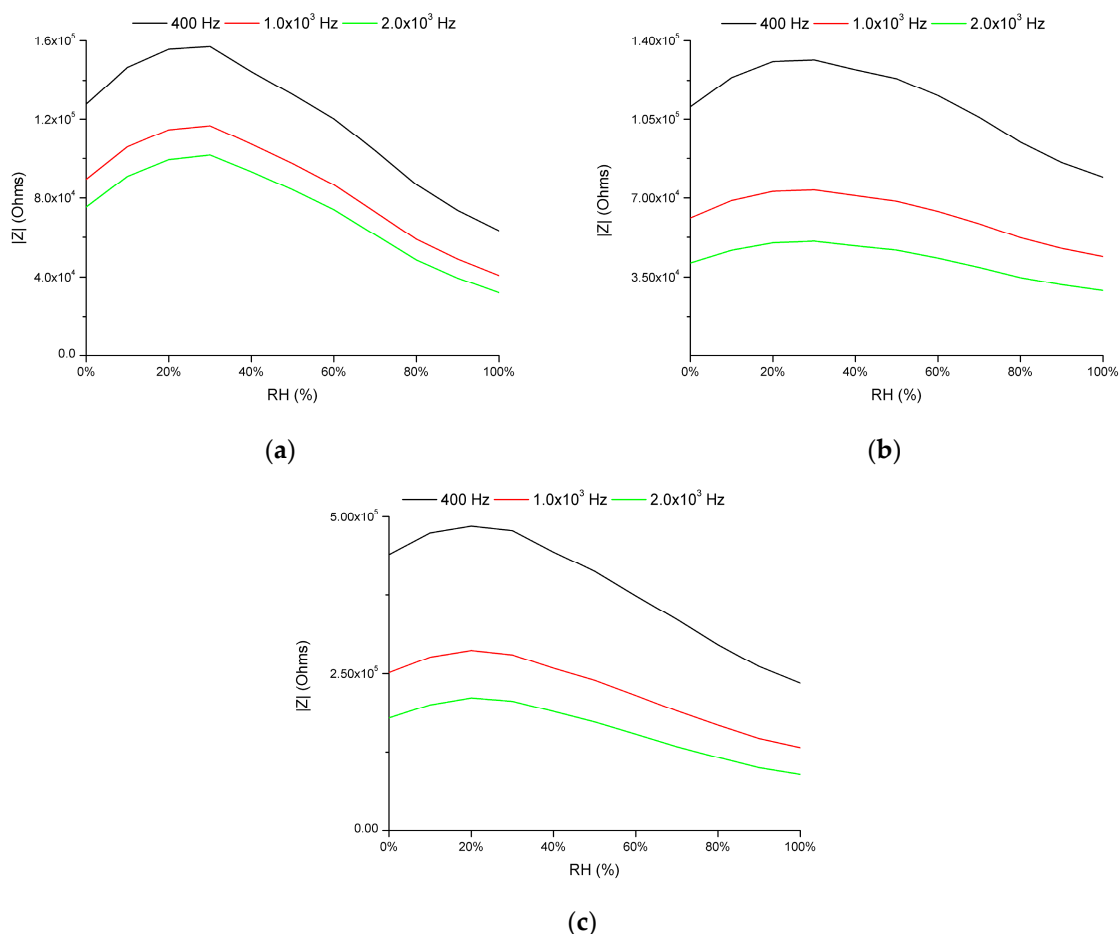
Figure 9. Impedance modulus variations with RH for three different excitation frequencies: (**a**–**c**) for PP20, PP15, and PP10 samples, respectively.

Indeed, (1) for all three samples' plots, it is reinforced that the *p*- to n-type conduction transition occurs at around 30% RH; (2) it is sample PP20 that exhibits an above 30% RH, the highest overall moduli variation, of around one order of magnitude.

In addition, from those plots, the additional conclusion to be retrieved is that lower excitation frequencies allow a higher sensitivity once for all samples; when higher excitation stimuli are evaluated, the overall modulus variation decreases. Nevertheless, this fact is in accordance with the high ionic nature of the samples, which is largely present, and its effect takes place at low frequencies.

The authors also evaluated the samples' electrical behavior with humidity ageing. Once the sample displaying the highest sensitivity was sample PP20, only the study carried out for this one is displayed here (see Figure 10) and discussed. The plotted spectra were taken with a 3-month difference. When comparing the obtained Nyquist plots and the calculated impedance modulus with varying humidity concentrations, it can be stated that the PP20 sample exhibits a relatively low ageing effect. Indeed, the obtained spectra for each RH concentration, collected with a 3-month difference, and the determined impedance modulus variation with RH, can be superposed with a degree of superposition higher than 90%. The ageing level can be better observed with Figure 10e, where a close comparison between the calculated impedance moduli based on the measures taken with a 3-month difference is displayed. The PP20 sample's estimated sensitivity in the 30–100% RH range is around 1.5 (the estimated values for the other samples, PP10 and PP15, are 0.65 and 0.55, respectively), with an impedance modulus variation with an RH slope of ~1.35 kΩ/%RH (sensitivity was determined by dividing the difference between the impedance moduli at 100 and 30% RH by the value of the impedance modulus at 30% RH, while the impedance variation with RH was determined by dividing the difference between the impedance moduli at 100 and 30% RH by the RH range in the evaluation).

Additionally, and when comparing to previous published results also obtained for PAA-based samples [40], obtained using a fluoroplastic-type binder, the present work's results, where PVA was used, allowed for enhancing moisture sensitivity and diminishing ageing (the estimated standard deviation using the determined impedance modulus traces for both periods is 5.7 kΩ, which is relatively low considering that the sensor impedance modulus varies mainly in the hundreds of the kΩ range). Indeed, a close comparison between the best results previously published (see Figure 11) and the finest ones from the present work (see Figure 10) allows for demonstrating the just-mentioned facts. In addition, and from the same sets of plots, it can be concluded that overall moisture sensitivity was increased; indeed, the overall impedance modulus variation above 30% RH was also increased, from around 0.4 to around one order of magnitude, at 400 Hz.

Once it was known that the impedance spectrums illustrate the diverse polarization and electrical phenomena that contribute to the overall response of the materials, the authors proceeded with the development of an equivalent circuit model, schematized in Figure 12, adapted from previously published works. The elements were chosen considering the previously carried out discussion of the electrical response of the samples to moisture, during which the authors already advanced a hypothesis regarding the contributions to their overall electrical response, hoping it would suit the under-study sensor samples. In a previous literature report, the authors discussed the humidity-sensing mechanisms behind PAA ionic conductors prepared using a fluoroplastic-type binder [40]. The mechanisms behind the present PAA samples prepared using PVA are the same, which is in line with the fact that the same electrical circuit model supports the discussion of the observed contributions in both works. In resume, at low RH concentrations, only chemisorption takes place, during which water molecules are firmly bonded to the surface of the chemisorbed layer (typically, this layer is complete at around RH = 30%, covering the entire material surface); at this stage, the contributions are mainly of an electronic nature. As RH concentration keeps increasing, the charge carriers start to transfer according to the Grotthuss chain mechanism through the bulk of PAA (the protons originate from the autoprotolysis of surface water molecules and/or from the distortion of O–H bonds, and are displaced along the hydrogen bonds from one water molecule to another); at this point, ionic contributions dominate. However, at low moisture concentrations, below 20%, the number of charge carriers is insufficient for an effective and fast charge transfer to take place; consequently, the electronic contribution plays an essential role in the overall sensor response.

From the plotted fittings, the adequation of the studied and developed equivalent model could be confirmed; without a doubt, both the Nyquist and Bode fits show a high agreement with the obtained experimental data; see Figures 13 and 14. For all samples,

Figure 13 displays the obtained experimental response to an RH concentration of 20% and their respective fitted curves with the proposed electrical equivalent circuit using Nyquist representations.

(**a**)

(**b**)

(**c**)

(**d**)

(**e**)
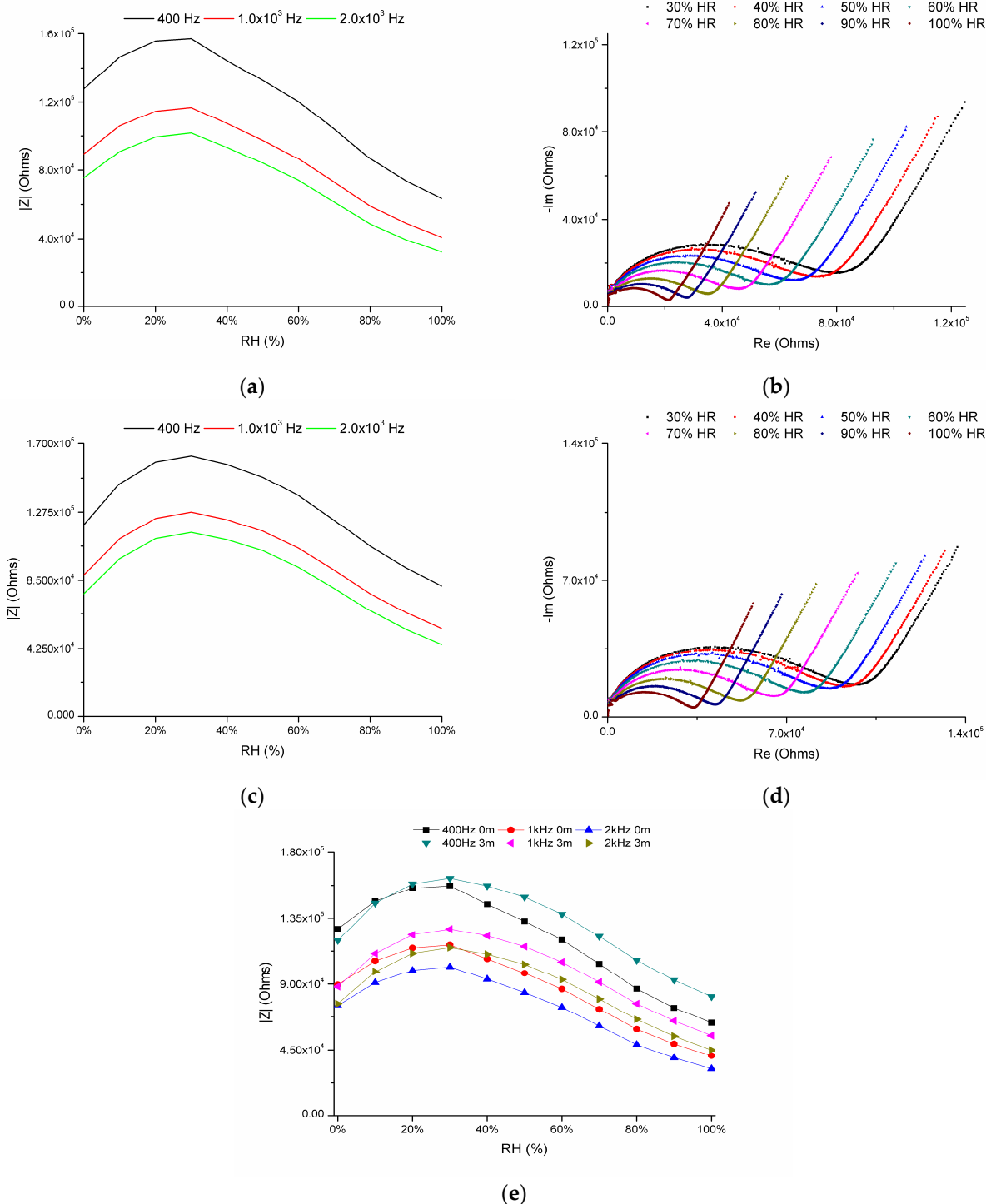
Figure 10. (**a**) Impedance modulus variations with RH for three different excitation frequencies for PP20 sample (first measurements); (**b**) RH-variation Nyquist plots for high-humidity range for PP20 sample (first measurements); (**c**) Impedance modulus variations with RH for three different excitation frequencies for PP20 sample, after 3 months; (**d**) RH-variation Nyquist plots for high-humidity range for PP20 sample, after 3 months; (**e**) Impedance modulus variations with RH for three different excitation frequencies for PP20 sample (comparison between first measurements and after 3 months).

(**a**)   (**b**)
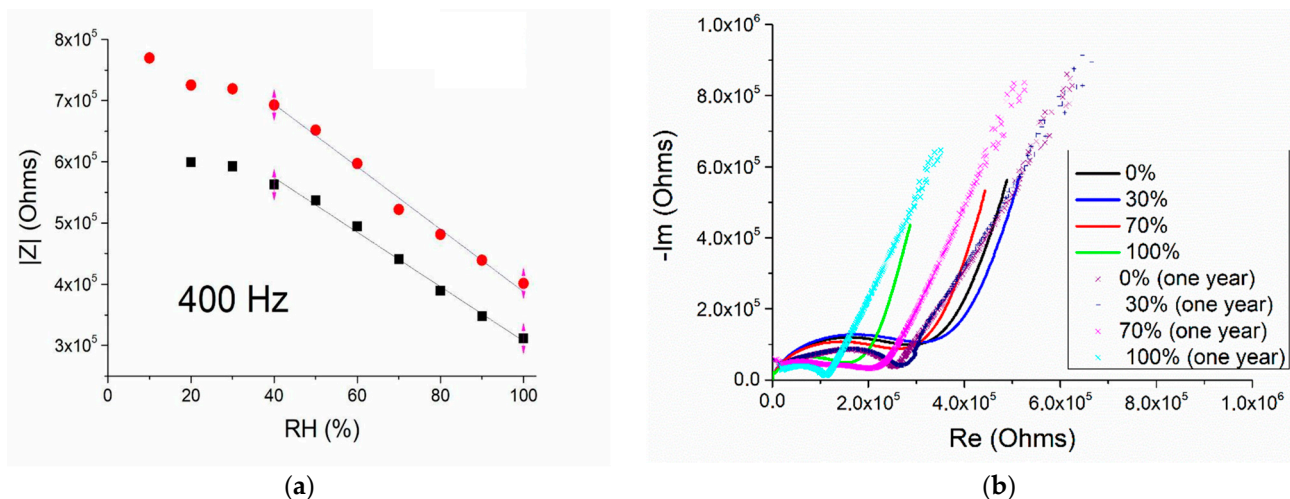
Figure 11. Electrical analysis of PAA samples fabricated using a fluoroplastic-type binder: (**a**) impedance modulus variation of PAA with RH; (**b**) Nyquist plots taken with 1-year difference [40].
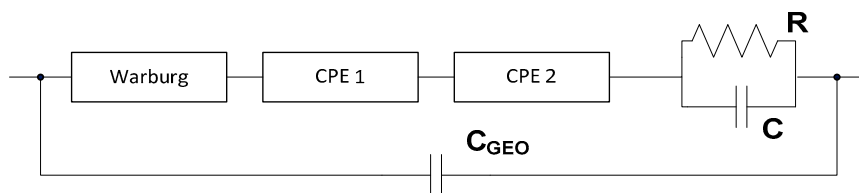
Figure 12. Electrical circuit equivalent model [40].

(**a**)   (**b**)

(**c**)
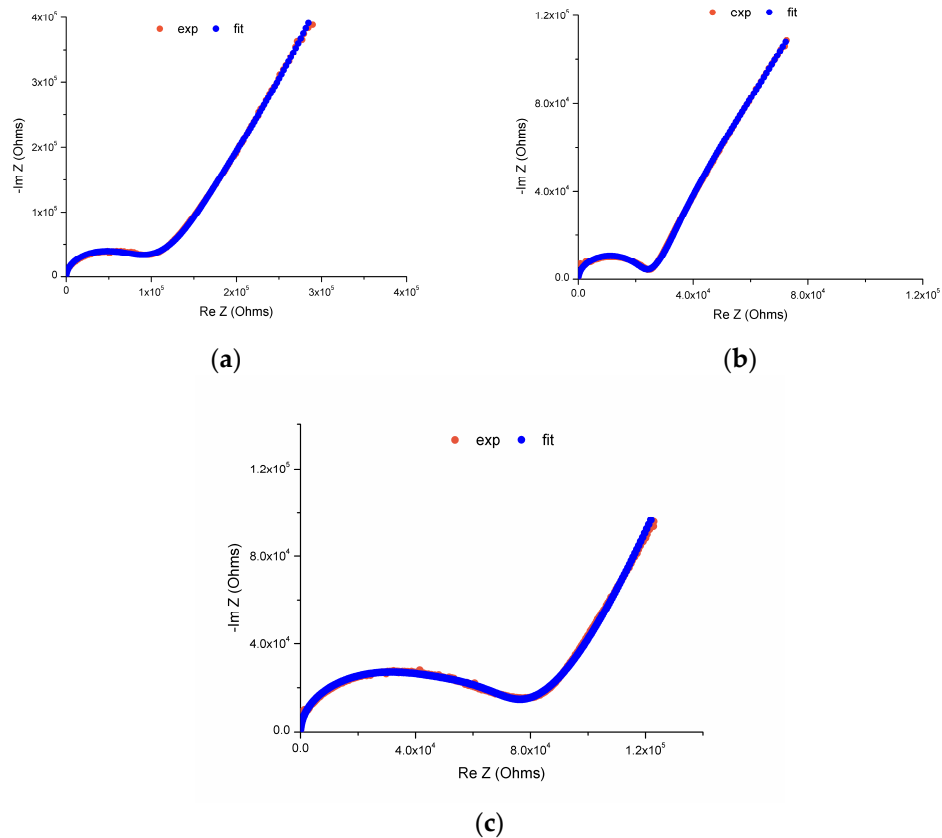
Figure 13. PP10, PP15, and PP20 Nyquist plots at 20% RH, and respective fitted curves, (**a–c**).

The level of superposition obtained is extremely high, proving that the chosen model is suitable for representing samples' electrical response to moisture. As discussed, the considered contributions are the following: (1) one element consisting of a resistor in parallel with a capacitor (representing the grain and grain agglomerates' contribution); (2) due to water coverage on the material surface, two constant phase elements are considered, CPE1 and CPE2, that stand for the charge diffusion contributions that take place at the interface between the electrodes and the material, and along grain boundaries; (3) a Warburg-type element, Warburg$_{coefficient}$, for representing the significant ionic diffusion contribution (the semi-infinite line visible in the Nyquist plots), which is mainly due to the surface paths for charge transport along the pores' surface and along pores that become gradually filled with water molecules; and (4) a geometric capacitance, Cgeo, that contemplates the geometric effects' contribution due to the electrodes' location, which are placed on the far ends of the upper faces of the samples (this placement resembles a capacitor with parallel plates).

Once the sample that exhibited better RH-variation sensitivity was PP20, Figure 14 is able to show additional Nyquist plots and respective fitted curves for RH concentrations of 0, 40, and 90% for the displayed moisture conditions to confirm how adequate the adopted model is; besides representing the Nyquist plots of both experimental and fitted curves, the bode plots of Real and Reactive components, of both experimental and fitted curves, are also shown.

Figure 14. *Cont.*

(**e**)

(**f**)

(**g**)

(**h**)

(**i**)
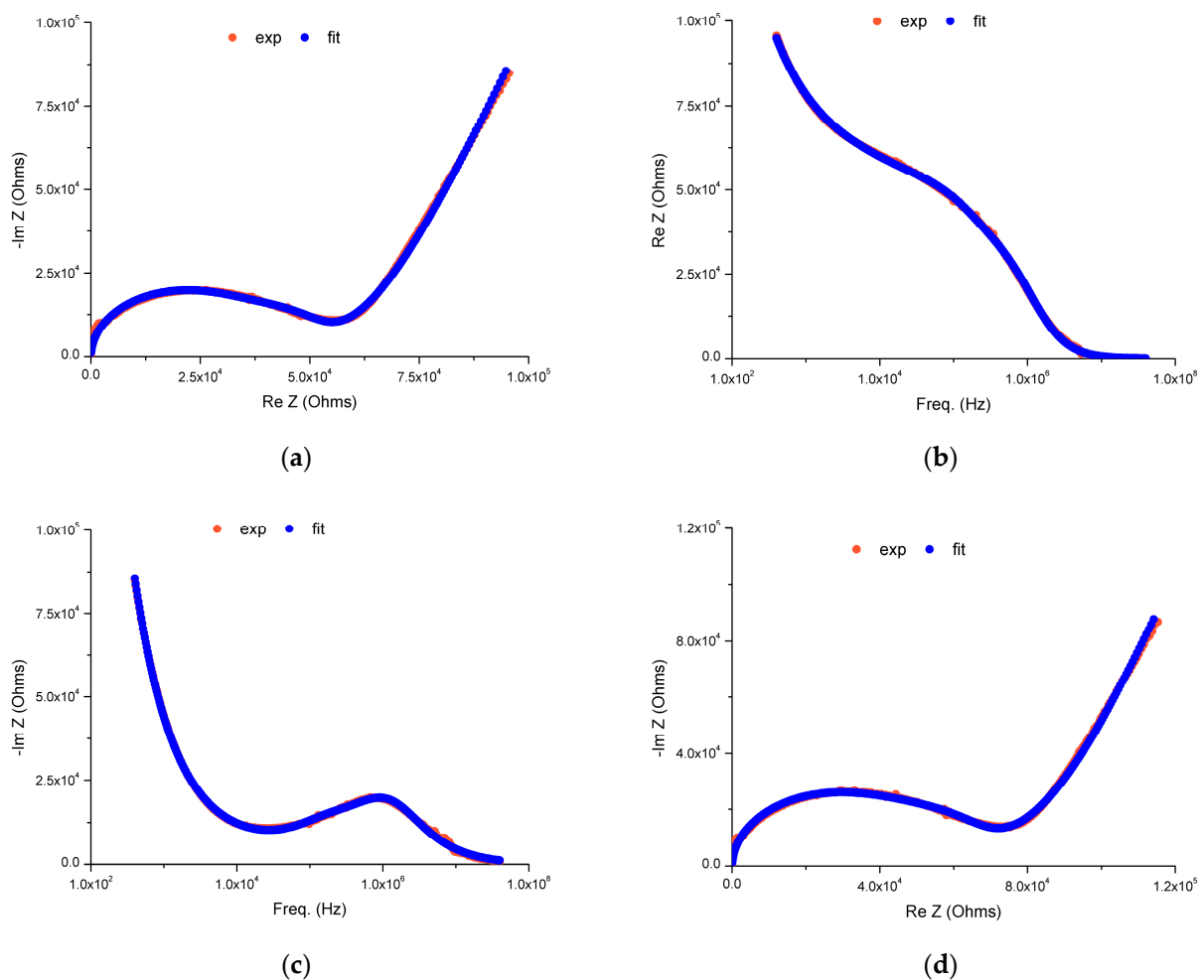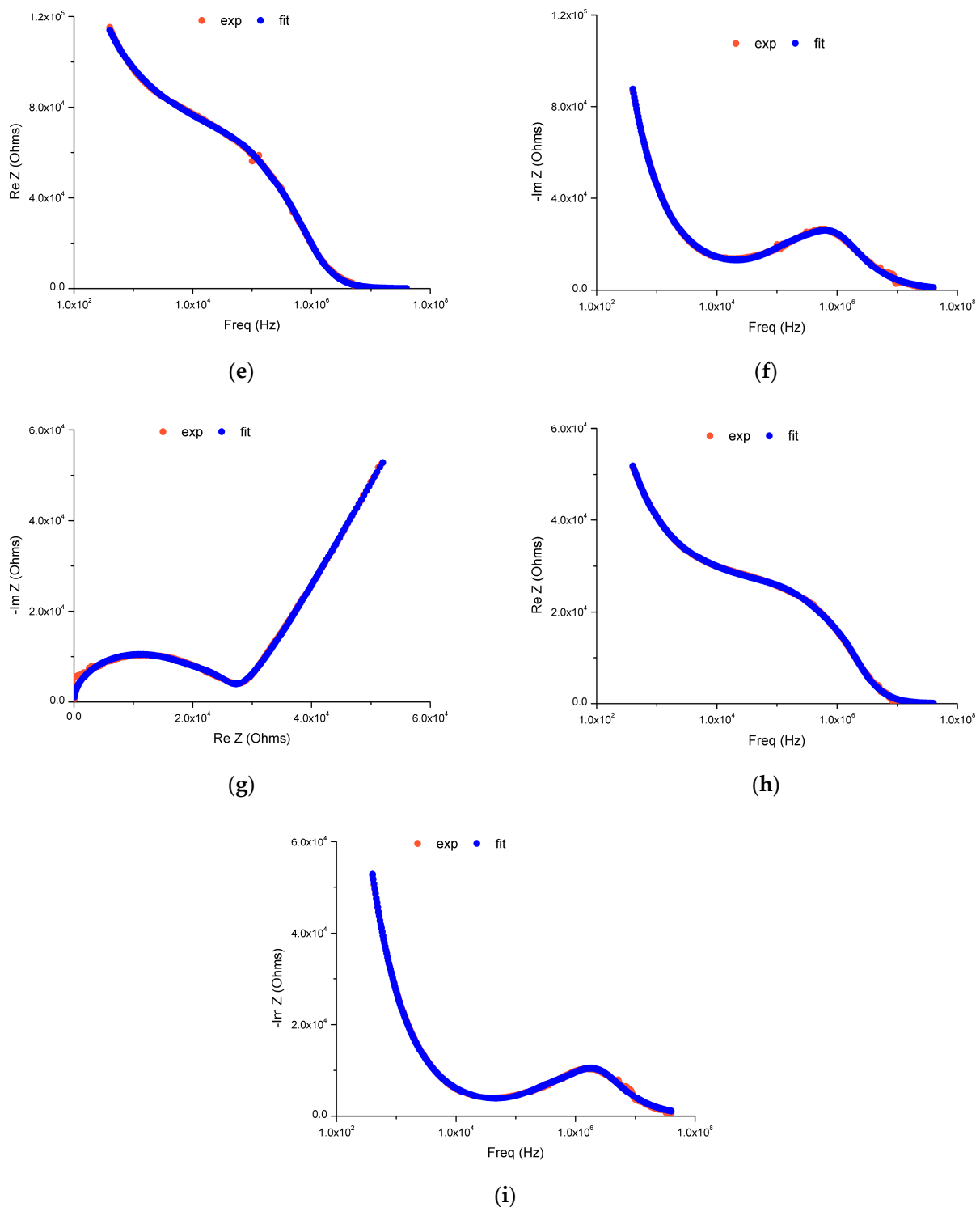
Figure 14. PP20 Nyquist and Bode plots (Real and Reactive components), containing their respective fitted curves, at 0, 40, and 90% RH, (**a**–**c**), (**d**–**f**), and (**g**–**i**), respectively.

Tables 1–3 display the obtained values for the electrical equivalent circuit model parameters. The determination of the first set of parameter values was carried out with EIS spectra analyzer software, following its manual fine-tuning. An analysis of the values in the tables allows for concluding that (1) the contribution due to grains/grain agglomerates of an electronic nature, characterized by the R//C element, decreases more than one order of magnitude when comparing samples PP10 and PP20 (PP20 is the sample that showed the

highest sensitivity). This is caused by the higher binder content of PP20, which raises the separation between the existent grains and agglomerates. In addition, for all samples, as RH concentration varies, a decreasing trend of the resistive component of this contribution is visible: the expected and observed reduction in the electronic contribution to the overall electric response of the sensors to moisture is responsible for this trend. (2) The considered geometric contribution effect, Cgeo, originating with the positioning of the measuring contacts, is confirmed. In addition, once the contribution values for all samples over the entire evaluated moisture range are pretty similar, their good adhesion to the sample's surface is also a fact. (3) For all compositions, the two CPE elements considered display different behaviors and values regarding a moisture increase; undeniably, regarding the CPE1 element, all samples display very similar values between them along the entire moisture range; the highest binder content sample, PP20, for the CPE2 component, exhibits admittance values that slightly decrease in the low-humidity range and that steadily increase in the high-humidity range, which are in agreement with the observed overall impedance modulus variation with RH concentration and in accordance with the found higher overall sensitivity to moisture changes. The two other samples also display admittance variation resembling that observed for PP20, but, in agreement with the observed lower sensitivity, with a lower overall variation in the case of PP15, or for PP10, attenuated by the variation of the power coefficient of the admittance. (4) The Warburg-type contribution coefficient displays values and differences in accordance with the slopes' variation due to the changes in the binder content and RH concentration, as seen in the Nyquist plots. Indeed, for PP20 and PP15 samples, the coefficients show minor variations along the RH range evaluated, in consonance with the slope changes with RH concentration in the Nyquist plots (more significant for PP10). However, their range is of the same order of magnitude, a power of -12, which is in agreement with almost unseen slope differences in the plots due to the amount of binder content. Nevertheless, for PP20 and for all RH concentrations, the slope observed in the plots does not change with RH concentration, and it is quite different from the one seen for the two other types of compositions; consequently, the Warburg coefficient also reflects these changes, displaying a power of -11, instead of -12.

For an easy assessment of the hysteresis level encountered for sample PP20, the impedance moduli estimated for data obtained from raising and decreasing RH-variation measures are plotted in Figure 15. The estimated standard deviation, after 3 months, was 6.8 kΩ, which can be considered low once the impedance modulus values vary mainly in the hundreds of the kΩ range (the determined hysteresis was below 6.8%).

Table 1. Fitted parameters for sample PP10 using the proposed equivalent circuit model.

RH (%)	R (Ω)	C (F)	Q_{CPE1} (S)	n_{CPE1} (a.u.)	Q_{CPE2} (S)	n_{CPE2} (a.u.)	Cgeo (F)	Wcoeffi. ($\Omega \times s^{-1/2}$)
0	2.77×10^4	9.11×10^{-9}	4.50×10^{-9}	8.29×10^{-1}	2.85×10^{-6}	1.19×10^{-1}	3.26×10^{-12}	8.31×10^{-12}
10	3.66×10^4	6.73×10^{-9}	3.81×10^{-9}	8.47×10^{-1}	2.30×10^{-6}	1.23×10^{-1}	3.26×10^{-12}	3.24×10^{-12}
20	4.07×10^4	6.27×10^{-9}	3.69×10^{-9}	8.50×10^{-1}	2.15×10^{-6}	1.22×10^{-1}	3.26×10^{-12}	9.41×10^{-12}
30	1.32×10^4	4.15×10^{-11}	6.10×10^{-9}	7.72×10^{-1}	3.40×10^{-6}	9.98×10^{-2}	3.07×10^{-12}	2.74×10^{-11}
40	9.30×10^2	4.86×10^{-11}	6.23×10^{-9}	7.79×10^{-1}	3.43×10^{-6}	9.64×10^{-2}	3.28×10^{-12}	2.72×10^{-12}
50	4.95×10^2	2.58×10^{-11}	6.59×10^{-9}	7.80×10^{-1}	3.87×10^{-6}	9.53×10^{-2}	3.28×10^{-12}	2.91×10^{-12}
60	6.51×10^3	5.17×10^{-11}	7.51×10^{-9}	7.71×10^{-1}	5.12×10^{-6}	9.42×10^{-2}	3.05×10^{-12}	20.0×10^{-12}
70	4.99×10^3	6.33×10^{-11}	8.62×10^{-9}	7.66×10^{-1}	6.53×10^{-6}	8.92×10^{-2}	3.08×10^{-12}	39.5×10^{-12}
80	2.81×10^3	9.04×10^{-11}	1.03×10^{-8}	7.58×10^{-1}	7.80×10^{-6}	8.87×10^{-2}	3.09×10^{-12}	42.2×10^{-12}
90	1.21×10^3	3.26×10^{-12}	1.19×10^{-8}	7.49×10^{-1}	1.00×10^{-5}	8.19×10^{-2}	3.29×10^{-12}	59.7×10^{-12}
100	1.03×10^2	1.28×10^{-12}	1.42×10^{-8}	7.44×10^{-1}	1.32×10^{-5}	7.07×10^{-2}	3.38×10^{-12}	86.6×10^{-12}

Table 2. Fitted parameters for sample PP15 using the proposed equivalent circuit model.

RH (%)	R (Ω)	C (F)	Q_{CPE1} (S)	n_{CPE1} (a.u.)	Q_{CPE2} (S)	n_{CPE2} (a.u.)	Cgeo (F)	Wcoeffi. ($\Omega \times s^{-1/2}$)
0	1.69×10^4	1.81×10^{-8}	2.46×10^{-8}	7.86×10^{-1}	3.15×10^{-5}	4.63×10^{-2}	3.69×10^{-12}	1.83×10^{-12}
10	2.01×10^4	1.60×10^{-8}	1.87×10^{-8}	8.09×10^{-1}	2.40×10^{-5}	4.96×10^{-2}	3.66×10^{-12}	7.23×10^{-12}
20	2.19×10^4	1.50×10^{-8}	1.64×10^{-8}	8.21×10^{-1}	2.09×10^{-5}	5.09×10^{-2}	3.66×10^{-12}	2.23×10^{-12}
30	2.15×10^4	1.51×10^{-8}	1.60×10^{-8}	8.23×10^{-1}	2.06×10^{-5}	5.05×10^{-2}	3.66×10^{-12}	1.74×10^{-12}
40	1.98×10^4	1.61×10^{-8}	1.70×10^{-8}	8.18×10^{-1}	2.22×10^{-5}	4.91×10^{-2}	3.65×10^{-12}	2.42×10^{-12}
50	1.86×10^4	1.70×10^{-8}	1.84×10^{-8}	8.11×10^{-1}	2.41×10^{-5}	4.79×10^{-2}	3.65×10^{-12}	1.01×10^{-12}
60	1.66×10^4	1.83×10^{-8}	2.09×10^{-8}	8.01×10^{-1}	2.81×10^{-5}	4.62×10^{-2}	3.66×10^{-12}	1.63×10^{-12}
70	1.39×10^4	2.07×10^{-8}	2.52×10^{-8}	7.85×10^{-1}	3.46×10^{-5}	4.34×10^{-2}	3.69×10^{-12}	1.85×10^{-12}
80	1.13×10^4	2.29×10^{-8}	3.09×10^{-8}	7.71×10^{-1}	4.51×10^{-5}	4.03×10^{-2}	4.00×10^{-12}	4.32×10^{-12}
90	9.34×10^3	2.59×10^{-8}	3.74×10^{-8}	7.57×10^{-1}	5.52×10^{-5}	3.69×10^{-2}	4.05×10^{-12}	3.05×10^{-12}
100	7.41×10^3	2.88×10^{-8}	4.17×10^{-8}	7.50×10^{-1}	7.03×10^{-5}	3.24×10^{-2}	4.18×10^{-12}	1.24×10^{-12}

Table 3. Fitted parameters for sample PP20 using the proposed equivalent circuit model.

| RH (%)	R (Ω)	C (F)	Q_{CPE1} (S)	n_{CPE1} (a.u.)	Q_{CPE2} (S)	n_{CPE2} (a.u.)	Cgeo (F)	Wcoeffi. ($\Omega \times s^{-1/2}$)
0	6.58×10^3	1.37×10^{-10}	2.15×10^{-8}	8.09×10^{-1}	9.36×10^{-6}	6.50×10^{-2}	3.35×10^{-12}	1.86×10^{-11}
10	7.93×10^3	1.30×10^{-10}	1.82×10^{-8}	8.23×10^{-1}	7.14×10^{-6}	6.98×10^{-2}	3.36×10^{-12}	1.33×10^{-11}
20	9.10×10^3	1.12×10^{-10}	1.66×10^{-8}	8.32×10^{-1}	6.24×10^{-6}	7.31×10^{-2}	3.50×10^{-12}	1.80×10^{-11}
30	9.05×10^3	1.08×10^{-10}	1.63×10^{-8}	8.37×10^{-1}	5.98×10^{-6}	7.41×10^{-2}	3.49×10^{-12}	4.13×10^{-11}
40	7.89×10^3	1.24×10^{-10}	1.88×10^{-8}	8.28×10^{-1}	6.79×10^{-6}	6.98×10^{-2}	3.49×10^{-12}	8.16×10^{-11}
50	6.91×10^3	1.35×10^{-10}	2.10×10^{-8}	8.19×10^{-1}	7.83×10^{-6}	6.71×10^{-2}	3.48×10^{-12}	9.45×10^{-11}
60	5.97×10^3	1.40×10^{-10}	2.41×10^{-8}	8.09×10^{-1}	9.34×10^{-6}	6.37×10^{-2}	3.50×10^{-12}	3.28×10^{-11}
70	5.03×10^3	1.45×10^{-10}	2.98×10^{-8}	7.92×10^{-1}	1.26×10^{-5}	5.65×10^{-2}	3.52×10^{-12}	8.04×10^{-11}
80	4.22×10^3	1.44×10^{-10}	3.89×10^{-8}	7.71×10^{-1}	1.89×10^{-5}	4.50×10^{-2}	3.56×10^{-12}	2.98×10^{-11}
90	3.57×10^3	1.27×10^{-10}	4.93×10^{-8}	7.54×10^{-1}	2.78×10^{-5}	3.42×10^{-2}	3.59×10^{-12}	2.74×10^{-11}
100	2.67×10^3	1.23×10^{-10}	5.81×10^{-8}	7.45×10^{-1}	3.91×10^{-5}	2.74×10^{-2}	3.66×10^{-12}	4.80×10^{-11}
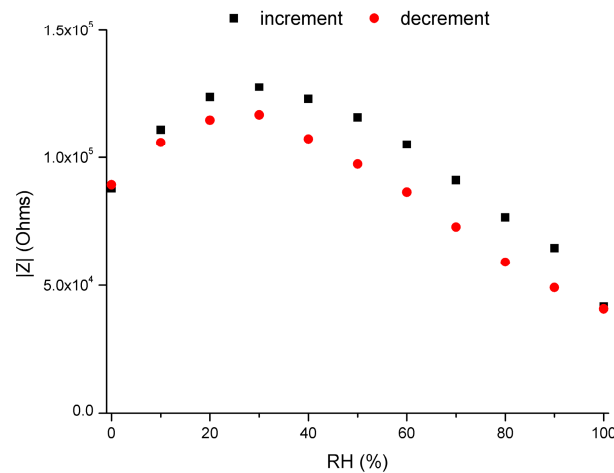
Figure 15. PP20-sample hysteresis evaluation.

For purposes of evaluating the outcomes of using this type of binder in the fabrication of humidity devices, the authors performed a comparison between their results based on the use of antimony and others published in the literature, which can be seen in Table 4.

Table 4. Literature data on the resistance of some humidity sensors.

Material Type	Resistance (Ohms)	RH Value (%)	Impedance (Ohms)	Hysteresis	Reference
$Sb_2O_5 \cdot 3H_2O$	8×10^4	10	1.4×10^5 (400 Hz)	low (<6.8%)	Present work
	3×10^4	90	8×10^4 (400 Hz)		
$Sb_2O_5 \cdot 3H_2O$	3×10^5	10	7.3×10^5 (400 Hz)	no	[40]
	1×10^5	90	3.5×10^5 (400 Hz)		
	3.2×10^5	90			
ZnO/SnO$_2$	-	25	10^7	yes	[43]
		90	10^4		
WS$_2$-modified SnO$_2$	195	30	-	no data	[44]
	225	90			
Porous TiO$_2$	-	10	5×10^5–10^8	no	[53]
		90	10^4		
Halloysite nanotubes	-	0	300	~5%	[10]
		91.5	5×10^5		
Silica nanoparticles	-	40	10^7	<6%	[9]
		90	8×10^9		
CS/ZnO/SWCNT composite	1.2×10^3	11	-	~10%	[54]
	3×10^3	97			

4. Conclusions

Using XRD, SEM, TEM, porosimetry, and EDS, the solid samples' structure and morphology were analyzed. It allowed for demonstrating that (1) the initial antimony powder used in the fabrication of the samples was entirely oxidated, i.e., pure antimony was synthesized; (2) the solid samples' mesoporosity exhibited levels that favor moisture adsorption/desorption; and (3) that the binder fills up the free spaces between the pure polyantimonic acid particles, allowing the direct transfer of protons through the bulk of the samples.

Electrical Impedance Spectroscopy data allowed the authors to conclude that the sensors prepared with PVA exhibit (1) a steady decrease in the total resistance and impedance modulus with moisture in the RH range between 30 and 90% and (2) that the use of PVA in comparison to fluoroplastic, used in a previous work, allowed for increasing moisture sensitivity, as well as the time stability of the electrical response of the sensors, while keeping hysteresis low.

The PP20 sensor was the one that displayed the highest moisture sensitivity as well as a low hysteresis and low electrical response ageing. If the just-mentioned facts are combined with the low fabrication cost, this allows the authors to state that PAA displays high future potential regarding its use for humidity detection/measurement. The authors will keep pursuing the study of other binders for the fabrication of a solid sensor, which

will enable sensitivity result enhancement, with the consequent use of PAA in up-to-market humidity-sensing devices.

Author Contributions: All authors contributed in equal parts to this article: conceptualization, P.F. and O.K.; investigation, S.M. and O.K.; formal analysis, S.M.; writing—original draft, S.M. and P.F.; writing—review and editing, P.F. and O.K. All authors have read and agreed to the published version of the manuscript.

Institutional Review Board Statement: Not applicable.

Data Availability Statement: Research data supporting the displayed results are not available due to ethical reasons.

Conflicts of Interest: The authors declare no conflict of interest.

References

1. Chen, Z.; Lu, C. Humidity Sensors: A Review of Materials and Mechanisms. *Sens. Lett.* **2005**, *3*, 274–295. [CrossRef]
2. Farahani, H.; Wagiran, R.; Hamidon, M.N. Humidity Sensors Principle, Mechanism, and Fabrication Technologies: A Comprehensive Review. *Sensors* **2014**, *14*, 7881–7939. [CrossRef] [PubMed]
3. Araújo, E.S.; Leão, V.N.S.; Monteiro, S.R.; Guimarães, R.P.; Barbosa, A.F.R.; Nascimento, M.M. Preparation of Ceramic Humidity Sensors by Electrospinning and Sintering: A Promising Alternative. *Res. Dev. Mater. Sci.* **2018**, *6*, 629–631. [CrossRef]
4. Morais, R.M.; dos Santos Klem, M.; Nogueira, G.L.; Gomes, T.C.; Alves, N. Low Cost Humidity Sensor Based on PANI/PEDOT:PSS Printed on Paper. *IEEE Sens. J.* **2018**, *18*, 2647–2651. [CrossRef]
5. Tulliani, J.-M.; Inserra, B.; Ziegler, D. Carbon-Based Materials for Humidity Sensing: A Short Review. *Micromachines* **2019**, *10*, 232. [CrossRef] [PubMed]
6. McGhee, J.R.; Sagu, J.S.; Southee, D.J.; Evans, P.S.A.; Wijayantha, K.G.U. Printed, Fully Metal Oxide, Capacitive Humidity Sensors Using Conductive Indium Tin Oxide Inks. *ACS Appl. Electron. Mater.* **2020**, *2*, 3593–3600. [CrossRef]
7. Zhu, Z.; Lin, W.-D.; Lin, Z.-Y.; Chuang, M.-H.; Wu, R.-J.; Chavali, M. Conductive Polymer (Graphene/PPy)–BiPO4 Composite Applications in Humidity Sensors. *Polymers* **2021**, *13*, 2013. [CrossRef]
8. Haq, Y.U.; Ullah, R.; Mazhar, S.; Khattak, R.; Qarni, A.A.; Haq, Z.U.; Amin, S. Synthesis and Characterization of 2D MXene: Device Fabrication for Humidity Sensing. *J. Sci. Adv. Mater. Devices* **2022**, *7*, 100390. [CrossRef]
9. Li, Z.; Wang, J.; Xu, Y.; Shen, M.; Duan, C.; Dai, L.; Ni, Y. Green and Sustainable Cellulose-Derived Humidity Sensors: A Review. *Carbohydr. Polym.* **2021**, *270*, 118385. [CrossRef] [PubMed]
10. Duan, Z.; Zhao, Q.; Wang, S.; Huang, Q.; Yuan, Z.; Zhang, Y.; Jiang, Y.; Tai, H. Halloysite Nanotubes: Natural, Environmental-Friendly and Low-Cost Nanomaterials for High-Performance Humidity Sensor. *Sens. Actuators B Chem.* **2020**, *317*, 128204. [CrossRef]
11. Duan, Z.; Zhao, Q.; Wang, S.; Yuan, Z.; Zhang, Y.; Li, X.; Wu, Y.; Jiang, Y.; Tai, H. Novel Application of Attapulgite on High Performance and Low-Cost Humidity Sensors. *Sens. Actuators B Chem.* **2020**, *305*, 127534. [CrossRef]
12. Duan, Z.; Jiang, Y.; Zhao, Q.; Wang, S.; Yuan, Z.; Zhang, Y.; Liu, B.; Tai, H. Facile and Low-Cost Fabrication of a Humidity Sensor Using Naturally Available Sepiolite Nanofibers. *Nanotechnology* **2020**, *31*, 355501. [CrossRef] [PubMed]
13. Najeeb, M.A.; Ahmad, Z.; Shakoor, R.A. Organic Thin-Film Capacitive and Resistive Humidity Sensors: A Focus Review. *Adv. Mater. Interfaces* **2018**, *5*, 1800969. [CrossRef]
14. Park, S.Y.; Lee, J.E.; Kim, Y.H.; Kim, J.J.; Shim, Y.-S.; Kim, S.Y.; Lee, M.H.; Jang, H.W. Room Temperature Humidity Sensors Based on RGO/MoS2 Hybrid Composites Synthesized by Hydrothermal Method. *Sens. Actuators B Chem.* **2018**, *258*, 775–782. [CrossRef]
15. Faia, P.M.; Libardi, J.; Louro, C.S. Effect of V_2O_5 Doping on P- to n-Conduction Type Transition of TiO_2:WO_3 Composite Humidity Sensors. *Sens. Actuators B Chem.* **2016**, *222*, 952–964. [CrossRef]
16. De Grotthuss, C.J.T. Sur La Décomposition de l'eau et Des Corps Qu'elle Tient En Dissolution à l'aide de l'électricité Galvanique. *Ann. Chim.* **1806**, *58*, 54–74.
17. England, W.; Cross, M.; Hamnett, A.; Wiseman, P.; Goodenough, J. Fast Proton Conduction in Inorganic Ion-Exchange Compounds. *Solid State Ion.* **1980**, *1*, 231–249. [CrossRef]
18. Delacroix, M.A.E. Acides Antimoniques et Antimoniates. *Bull. Soc. Chim. Fr.* **1899**, *21*, 1049–1054.
19. Senderens, M.J.B. Sur Un Nouvel Acide Antimonique Soluble et Ses Antimoniates. *Bull. Soc. Chim. Fr.* **1899**, *21*, 47–58.
20. Abe, M.; Ito, T. Synthetic Inorganic Ion-Exchange Materials. X. Preparation and Properties of So-Called Antimonic(V) Acid. *Bull. Chem. Soc. Jpn.* **1968**, *41*, 333–342. [CrossRef]

21. Mayer, S.F.; Rodrigues, J.E.; Sobrados, I.; Gainza, J.; Fernández-Díaz, M.T.; Marini, C.; Asensio, M.C.; Alonso, J.A. Synergy of Diffraction and Spectroscopic Techniques to Unveil the Crystal Structure of Antimonic Acid. *Sci. Rep.* **2021**, *11*, 17763. [CrossRef] [PubMed]

22. Kosohin, O.; Matvieiev, O.; Linyucheva, O. Hydrated Antimonic Acid as a Solid Electrolyte. *Mater. Today Proc.* **2022**, *50*, 521–523. [CrossRef]

23. Tourky, A.R.; Mousa, A.A. 150. Studies on Some Metal Electrodes. Part V. The Amphoteric Properties of Antimony Tri- and Pent-Oxide. *J. Chem. Soc.* **1948**, *0*, 759–763. [CrossRef]

24. Ostrovskii, D.; Valakh, M.; Karasiova, T.; Yaremko, A. The Peculiarities of Hydrogen Bonds in Raman Spectra of Solid Superionic Polyantimonic Acids. *Ferroelectrics* **1997**, *192*, 93–99. [CrossRef]

25. Baetsle, L.H.; Huys, D. Structure and Ion-Exchange Characteristics of Polyantimonic Acid. *J. Inorg. Nucl. Chem.* **1968**, *30*, 639–649. [CrossRef]

26. Burmistrov, V.A.; Kovalenko, L.Y.; Firsova, O.A.; Filonenko, E.M.; Lupitskaya, Y.A. Ion Transport in Hydrated Compounds Based on Crystalline Polyantimonic Acid. *Butlerov Commun.* **2020**, *62*, 80–84. [CrossRef]

27. Jander, G.; Simon, A. Zur Kenntnis Der Antimonpentoxydhydrate. *Z. Anorg. Allg. Chem.* **1923**, *127*, 68–82. [CrossRef]

28. Pauling, L. The Formulas of Antimonic Acid and the Antimonates. *J. Am. Chem. Soc.* **1933**, *55*, 1895–1900. [CrossRef]

29. Belinskaya, F.A.; Militsina, E.A. Inorganic Ion-Exchange Materials Based on Insoluble Antimony(V) Compounds. *Russ. Chem. Rev.* **1980**, *49*, 933–952. [CrossRef]

30. Leysen, R.; Vandenborre, H. Synthesis and Characterization of Polyantimonic Acid Membranes. *Mater. Res. Bull.* **1980**, *15*, 437–450. [CrossRef]

31. Yaroshenko, F.A.; Burmistrov, V.A. Dielectric Relaxation and Protonic Conductivity of Polyantimonic Crystalline Acid at Low Temperatures. *Russ. J. Electrochem.* **2015**, *51*, 391–396. [CrossRef]

32. Yaroshenko, F.A.; Burmistrov, V.A. Dielectric Losses and Proton Conductivity of Polyantimonic Acid Membranes. *Russ. J. Electrochem.* **2016**, *52*, 690–693. [CrossRef]

33. Yaroshenko, F.A.; Burmistrov, V.A. Synthesis of Hybrid Materials Based on MF-4SK Perfluorinated Sulfonated Cation-Exchange Membranes Modified with Polyantimonic Acid and Characterization of Their Proton Conductivity. *Pet. Chem.* **2018**, *58*, 770–773. [CrossRef]

34. Lan, Z.; Ji-Ying, W.; Xuan, Z.; Fu-Zhi, L.; Feng, J. Preparation, Characterization and Sr(II) Adsorption Performance of Self-Doped Antimony Oxide. *Acta Phys. Chim. Sin.* **2014**, *30*, 1923–1931. [CrossRef]

35. Lefebvre, J. L'acide Antimonique Échangeur d'ions. Mise En Évidence et Nature Des Échanges. *C R. Hebd. Seances Acad. Sci.* **1965**, *260*, 5575–5578.

36. Kurapova, O.Y.; Faia, P.M.; Zaripov, A.A.; Pazheltsev, V.V.; Glukharev, A.A.; Konakov, V.G. Electrochemical Characterization of Novel Polyantimonic-Acid-Based Proton Conductors for Low- and Intermediate-Temperature Fuel Cells. *Appl. Sci.* **2021**, *11*, 11877. [CrossRef]

37. Amarilla, J. Antimonic Acid and Sulfonated Polystyrene Proton-Conducting Polymeric Composites. *Solid. State Ion.* **2000**, *127*, 133–139. [CrossRef]

38. Leysen, R.; Doyen, W.; Proost, R.; Vermeiren, P.; Adriansens, W.; Deknock, R. The Use of Heterogeneous Membranes in Electrochemical Systems. In *Synthetic Polymeric Membranes*; Sedláček, B., Kahovec, J., Eds.; De Gruyter: Berlin, Germany; Boston, MA, USA, 1987; pp. 89–100.

39. Vandenborre, H.; Leysen, R.; Baetslé, L. Alkaline Inorganic-Membrane-Electrolyte (IME) Water Electrolysis. *Int. J. Hydrogen Energy* **1980**, *5*, 165–171. [CrossRef]

40. Mendes, S.; Kurapova, O.; Faia, P.; Pazheltsev, V.; Zaripov, A.; Konakov, V. Polyantimonic Acid-Based Materials Evaluated as Moisture Sensors at Ambient Temperature. *J. Solid State Electrochem.* **2023**, *27*, 611–625. [CrossRef]

41. Mohseni Kiasari, N.; Soltanian, S.; Gholamkhass, B.; Servati, P. Room Temperature Ultra-Sensitive Resistive Humidity Sensor Based on Single Zinc Oxide Nanowire. *Sens. Actuators A Phys.* **2012**, *182*, 101–105. [CrossRef]

42. Chang, S.-P.; Chang, S.-J.; Lu, C.-Y.; Li, M.-J.; Hsu, C.-L.; Chiou, Y.-Z.; Hsueh, T.-J.; Chen, I.-C. A ZnO Nanowire-Based Humidity Sensor. *Superlattices Microstruct.* **2010**, *47*, 772–778. [CrossRef]

43. Li, F.; Li, P.; Zhang, H. Preparation and Research of a High-Performance ZnO/SnO2 Humidity Sensor. *Sensors* **2021**, *22*, 293. [CrossRef] [PubMed]

44. Chen, Y.; Pei, Y.; Jiang, Z.; Shi, Z.; Xu, J.; Wu, D.; Xu, T.; Tian, Y.; Wang, X.; Li, X. Humidity Sensing Properties of the Hydrothermally Synthesized WS2-Modified SnO2 Hybrid Nanocomposite. *Appl. Surf. Sci.* **2018**, *447*, 325–330. [CrossRef]

45. Kovalenko, L.Y.; Yaroshenko, F.A.; Burmistrov, V.A.; Isaeva, T.N.; Galimov, D.M. Thermolysis of Hydrated Antimony Pentoxide. *Inorg. Mater.* **2019**, *55*, 586–592. [CrossRef]

46. Kovalenko, L.Y.; Burmistrov, V.A.; Zakhar'evich, D.A.; Kalganov, D.A. On the Mechanism of Proton Conductivity of Polyantimonic Acid. *Chelyabinsk Phys. Math. J.* **2021**, *6*, 95–110. [CrossRef]

47. Shabana, E.I.; El-Dessouky, M.I.; Abed El-Aziz, M.M. The Ion Exchange Characteristics of Antimonic Acid. *J. Radioanal. Nucl. Chem.* **2002**, *251*, 293–296. [CrossRef]

48. Yu, T.; Zhang, H.; Cao, H.; Zheng, G. Understanding the Enhanced Removal of Bi(III) Using Modified Crystalline Antimonic Acids: Creation of a Transitional Pyrochlore-Type Structure and the Sb(V)-Bi(III) Interaction Behaviors. *Chem. Eng. J.* **2019**, *360*, 313–324. [CrossRef]

49. Yu, T.; Shen, Y.; Zhang, H.; Xu, S.; Cao, H.; Zheng, G. Efficient Removal of Bismuth with Supersoluble Amorphous Antimony Acids: An Insight into Synthesis Mechanism and Sb(V)-Bi(III) Interaction Behaviors. *Chem. Eng. J.* **2021**, *420*, 127617. [CrossRef]

50. Wang, B.; Deng, Z.; Xia, Y.; Hu, J.; Li, H.; Wu, H.; Zhang, Q.; Zhang, Y.; Liu, H.; Dou, S. Realizing Reversible Conversion-Alloying of Sb(V) in Polyantimonic Acid for Fast and Durable Lithium- and Potassium-Ion Storage. *Adv. Energy Mater.* **2020**, *10*, 1903119. [CrossRef]

51. Bauerle, J.E. Study of Solid Electrolyte Polarization by a Complex Admittance Method. *J. Phys. Chem. Solids* **1969**, *30*, 2657–2670. [CrossRef]

52. Barsoukov, E.; Macdonald, J.R. *Impedance Spectroscopy: Theory, Experiment, and Applications*, 3rd ed.; Barsoukov, E., Macdonald, J.R., Eds.; John Wiley & Sons, Inc.: Hoboken, NJ, USA, 2018; ISBN 9781119381860.

53. Wang, Z.; Shi, L.; Wu, F.; Yuan, S.; Zhao, Y.; Zhang, M. The Sol–Gel Template Synthesis of Porous TiO_2 for a High Performance Humidity Sensor. *Nanotechnology* **2011**, *22*, 275502. [CrossRef] [PubMed]

54. Dai, H.; Feng, N.; Li, J.; Zhang, J.; Li, W. Chemiresistive humidity sensor based on chitosan/zinc oxide/single-walled carbon nanotube composite film. *Sens. Actuators B Chem.* **2020**, *283*, 786–792. [CrossRef]